



Noble-metal-free hetero-structural CdS/Nb₂O₅/N-doped-graphene ternary photocatalytic system as visible-light-driven photocatalyst for hydrogen evolution

Zongkuan Yue^a, Aijun Liu^a, Chunyong Zhang^a, Jie Huang^{a,b}, Mingshan Zhu^{c,*}, Yukou Du^a, Ping Yang^{a,*}

^a College of Chemistry, Chemical Engineering and Materials Science, Soochow University, Suzhou 215123, China

^b Key Laboratory of Nano-Bio Interface, Division of Nanobiomedicine, Suzhou Institute of Nano-Tech and Nano-Bionics, Chinese Academy of Sciences, Suzhou 215123, China

^c The Institute of Scientific and Industrial Research (SANKEN), Osaka University, Osaka 567-0047, Japan

ARTICLE INFO

Article history:

Received 14 June 2016

Received in revised form 8 August 2016

Accepted 15 August 2016

Available online 16 August 2016

Keywords:

Noble-metal-free

Visible-light-driven

CdS/Nb₂O₅/N-doped-graphene

ABSTRACT

In this paper, visible-light-driven photocatalysts composed of CdS nanoparticles, Nb₂O₅ nanorods (NbR) and N-doped graphene (NGR) nanosheets for photocatalytic water reduction to produce hydrogen have been synthesized. Under visible light irradiation, the prepared ternary nanocomposites showed distinctly enhanced photocatalytic performance for hydrogen evolution compared to bare CdS, NbR and CdS/Nb₂O₅. The sample with 2 wt.% NGR exhibited the highest photocatalytic activity, which is ca. 7.7 times as high as that evolved from CdS. The enhancement of photocatalytic performance may be related to the unique one dimension (1D) Nb₂O₅ structure with high surface-to-volume ratio, which can provide intimate interfacial contact between NbR and CdS nanoparticles, as well as the CdS/Nb₂O₅ heterojunction structure and two dimension (2D) NGR, which enhance the separation efficiency of photogenerated charge carriers. This work provides a promising and cost-effective method by combining the 0D CdS nanoparticles, 1D Nb₂O₅ nanorods and 2D N-doped graphene to form a ternary photocatalytic system for highly efficient hydrogen evolution from water without using any noble metals.

© 2016 Elsevier B.V. All rights reserved.

1. Introduction

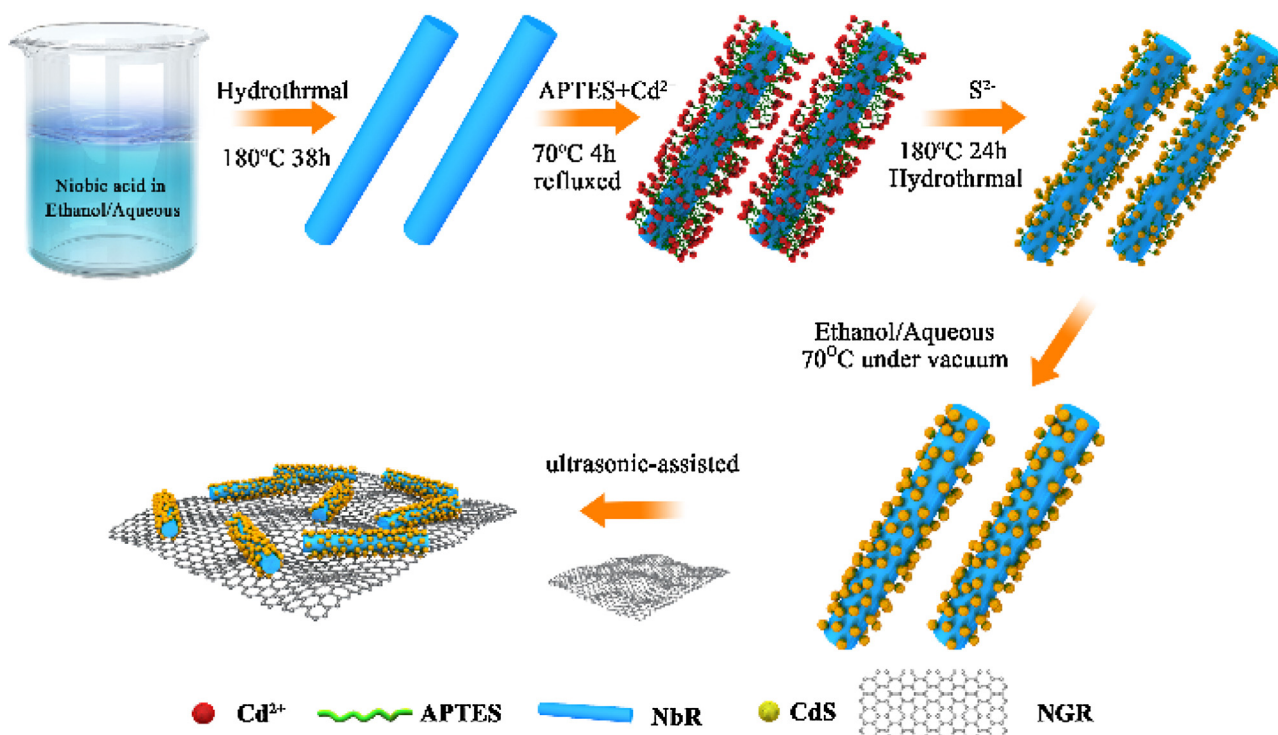
Over the past decades, semiconductor-based photocatalysts have attracted great attention due to their applications in solar energy conversion and environmental remediation [1,2]. The direct conversion of solar energy to chemical energy by means of photocatalytic water splitting to produce hydrogen is considered as one of the most promising green methods [3–5]. To date, a large number of semiconductor materials have been studied for such a process [6,7], however, stable and highly efficient visible-light-driven photocatalysts for hydrogen production under solar-light irradiation are still scarce. Therefore, development of efficient visible-light-driven photocatalysts for renewable energy production is highly desired. Cadmium sulfide (CdS), as an *n*-type semiconductor with a narrow band gap, has been considered as a fascinating visible-light-driven

photocatalyst for hydrogen evolution [8–11]. However, CdS has its own intrinsic defects, such as low activity for hydrogen production and relatively low stability toward photocorrosion, which limit its practical applications. Hence, considerable efforts have been dedicated to either enhancing photocatalytic activity or inhibiting the photocorrosion of CdS [12–17]. For example, coupling CdS with various semiconductors (e.g. TiO₂ [12,13], ZnO [14–16], TaON [17], etc.) has been shown to be an effective method to alter the energy levels of the conduction and valence bands of the photocatalytic systems. Through formation heterojunction structures, which accelerates the separation of photogenerated charge carriers and prevents the electron-hole recombination [18], the photocatalytic performance of the catalysts is greatly improved.

Recently, one dimensional (1D) Nb₂O₅ nanomaterials, such as nanotubes [19], nanorods [20], nanobelts [21], have been synthesized and used as photocatalysts because of their unique 1D nanostructure and promising functions. For example, Xue et al. verified that Nb₂O₅ nanorods (NbR) with high surface-to-volume ratio and single crystal structure could provide a direct path for photoinduced charges transfer, resulting in enhanced photocatalytic

* Corresponding authors.

E-mail addresses: mingshanzhu@yahoo.com (M. Zhu), pyang@sdu.edu.cn (P. Yang).



Scheme 1. Scheme of the fabrication process of CNG nanocomposites.

activity [20]. Considering merits of both Nb_2O_5 and CdS, we suppose that hybridization 1D NbR with CdS may produce a novel hybrid with enhanced photocatalytic performance. Since these two materials possess different band levels, the photoexcited electron generated from CdS can be transferred to 1D NbR, which will prevent the recombination of electron-hole. However, to the best of our knowledge, coupling CdS with Nb_2O_5 nanorods as a photocatalyst has not been reported yet.

On another front, N-doped graphene (NGR) as a famous cousin of graphene has received particular attentions in various photocatalytic applications [22–25]. Up to now, both theoretical and experimental results have demonstrated that NGR not only possesses superior electronic and chemical properties but also as a novel support of semiconductors, the strong coupling between catalytic components and the carrier enhances the interfacial contact, which in turn improves the efficiency of the photoinduced charge transfer and separation [26–29]. Thus, combination NGR with semiconductors or semiconductor composites may develop a new kind of energy conversion materials.

Herein, we report a novel ternary hetero-structural nanocomposite by combining the 0D CdS nanoparticles, 1D Nb_2O_5 nanorods and 2D N-doped graphene. The nanocomposite was tested as noble-metal-free photocatalyst for catalytic water reduction to produce hydrogen. Compared to bare CdS, NbR and $\text{CdS}/\text{Nb}_2\text{O}_5$, the fabricated ternary composites exhibited excellent stability and photocatalytic activity for photocatalytic hydrogen evolution. The enhanced photocatalytic performance of the nanocomposite can be attributed to unique 1D Nb_2O_5 structure, which can provide a direct path for photoinduced charges transfer, as well as the $\text{CdS}/\text{Nb}_2\text{O}_5$ heterojunction structure, which enhances the separation of photogenerated electron-hole pairs. Moreover, 2D NGR component in the nanocomposite acting as an electron acceptor and transporter promotes the rate of charger transfer greatly. This work demonstrates a promising and cost-effective method for constructing an effective photocatalyst without using any noble metals.

2. Experimental section

2.1. Materials

Niobium oxide (Nb_2O_5 , 99.99%), hydrofluoric acid (HF, 20 wt.%), ammonium hydroxide ($\text{NH}_3 \cdot \text{H}_2\text{O}$, 25–28 wt.%), cadmium acetate dihydrate ($\text{Cd}(\text{CH}_3\text{COO})_2 \cdot 2\text{H}_2\text{O}$), sodium sulfide nonahydrate ($\text{Na}_2\text{S} \cdot 9\text{H}_2\text{O}$) and 3-aminopropyl-triethoxysilane ($\text{C}_9\text{H}_{23}\text{NO}_3\text{Si}$, APTES) were obtained from Sinopharm Chemical Reagent Co., Ltd. (Shanghai, China). N-doped graphene was obtained from XFNANO Materials Tech. Co. (Nanjing, China). All reagents were analytical grade and used without further purification.

2.2. Preparation of Nb_2O_5 nanorods, CdS nanoparticles decorated Nb_2O_5 nanorod ($\text{CdS}/\text{Nb}_2\text{O}_5$) and $\text{CdS}/\text{Nb}_2\text{O}_5$ functionalized N-doped graphene (CNG) composites.

The fabrication process of CNG composite is shown as Scheme 1. Firstly, Nb_2O_5 nanorods (NbR) were prepared through the hydrothermal treatment using niobic acid as the starting materials. Niobic acid was prepared from Nb_2O_5 according to the method reported by Luo's group [30]. In a typical experiment, 0.1 g of niobic acid was dispersed into 40 mL of ethanol aqueous solution ($V_{\text{EtOH}}/V_{\text{H}_2\text{O}} = 1$). The suspension was added in a Teflon-lined stainless steel autoclave, heated to 180 °C and kept at the temperature for 38 h. After reaction, the mixture was naturally cooled down to room temperature. White precipitate was obtained by centrifugation, rinsed with deionized water and ethanol for several times. The sample was calcined at 600 °C for 5 h in air, obtaining Nb_2O_5 nanorods.

CdS nanoparticles (NPs) decorated Nb_2O_5 nanorods were prepared by a hydrothermal method. To 20 mL of ethanol, 0.1 g of Nb_2O_5 nanorods and 0.2 mL of 3-aminopropyl-triethoxysilane (APTES) as a ligand for immobilization of Cd^{2+} were added under ultrasonication. The mixture was heated under reflux for 3 h, then, was cooled down to room temperature. To the mixture, first

calculated amount of $\text{Cd}(\text{CH}_3\text{COO})_2$ solution (1 mg mL^{-1}), then, stoichiometric Na_2S solution (25 mg mL^{-1}) was dropwise added and stirred at room temperature for 2 h. The mixture was transferred to an 80 mL Teflon-lined autoclave and heated at 180°C for 24 h. The solid was isolated from the mixture by centrifugation, and washed with deionized water and ethanol for several times. The obtained solid was dried at 70°C under vacuum, then, was annealed in Ar at 600°C for 2 h with a heating rate of $10^\circ\text{C min}^{-1}$. The resultant samples were stored in darkness before further processing. For convenience, the resulting CdS nanoparticles decorated Nb_2O_5 nanorods were labelled as CN_x , where x stands for the weight percentage of CdS in the nanohybrid, $x = 0, 5, 10, 20$ and 40 .

The modification of $\text{CdS}/\text{Nb}_2\text{O}_5$ with N-doped graphene (NGR) hybrids was carried out by a self-assembly method under ultrasonic treatment. Typically, 0.1 g of CN_{20} sample and an appropriate amount of the NGR colloidal suspension (0.1 mg mL^{-1}) were mixed with 40 mL of deionized water and the mixture was ultrasonicated for 12 h. After that, the solvent was removed using a rotary evaporator at 40°C . The as-prepared sample was labelled as CN_xG_y , where y stands for the weight percent of NGR in the nanocomposite, $y = 0, 1, 2, 4$ and 6 . All samples were stored in darkness before used for the photocatalytic reactions. For comparison, CdS NPs modified NGR (labeled as CG_2 , i.e. 2wt.% NGR) and CdS NPs modified Nb_2O_5 NPs were also prepared by the same hydrothermal method.

2.3. Characterization

The wide angle ($2\theta = 20 - 80^\circ$) X-ray diffraction (XRD) patterns of all samples were collected on a Philips diffractometer using Ni-filtered $\text{Cu K}\alpha$ radiation. Scanning electron microscopy (SEM) measurements were performed on an SEM Hitachi S-4700. High resolution transmission electron microscopy (HRTEM) investigations were performed on a Tecnai G2 F20 S-TWIN instrument. Scanning transmission electron microscope (STEM) images were obtained using a Tecnai G2 F20 electron microscope operating at an accelerating voltage of 200 kV . Raman spectra of the samples were measured with a Jobin Yvon HR-800 spectrometer using a He-Ne laser ($\lambda = 633 \text{ nm}$, spot size $\sim 1 \mu\text{m}$). X-ray photoelectron spectroscopy (XPS) measurements were taken by an AXIS Ultra DLD system (Kratos Analytical Inc.) using monochromatic Al K α radiation. Binding energies were calculated with respect to C1 s at 284.5 eV . UV-vis diffuse reflectance spectra (DRS) of the samples were measured on a UV-1800 SPC spectrophotometer. Photoelectrochemical measurements of the samples were carried out on a CHI 660 D potentiostat/galvanostat electrochemical analyzer in a three-electrode system consisting of an indium tin oxide (ITO) glass covered with the sample acted as the working electrode, the platinum wire as the counter electrode, and a saturated calomel electrode (SCE) as the reference electrode. The electrodes were immersed in 0.2 M of Na_2SO_4 solution. The working electrode was irradiated with a GY-10 xenon lamp during the measurement. Electrochemical impedance spectroscopy (EIS) displayed as a Nyquist plot was carried out in the frequency range of 1 Hz to 10^5 Hz with an AC perturbation signal of 5 mV . The Mott-Schottky (M-S) plots were measured with a frequency of 1000 Hz . The flat band potential of the semiconductors was calculated by the M-S Eq. (1) [31]:

$$\frac{1}{C^2} = \frac{2}{e\epsilon\epsilon_0 N_d} \times (E - E_{fb} - \frac{kT}{e}) \quad (1)$$

where C is the capacitance of the electrode, e is the elementary charge, ϵ is the dielectric constant of the electrode material, ϵ_0 is permittivity of vacuum, N_d is the donor density, E is the applied potential, k is Boltzmann constant and T is the temperature. The potential of flat band (E_{fb}) is determined by the intercept of the potential axis, which obtained by fitting the liner to the plot. For converting the measured potential vs. SCE to the potential vs.

reversible hydrogen electrode (RHE), the following Nernst equation [32]:

$$E_{\text{RHE}} = E_{\text{SCE}} + 0.059\text{pH} + E_{\text{SCE}}^\circ \quad (2)$$

where E_{RHE} is the potential vs. RHE, E_{SCE} is the measured potential vs. SCE, and $E_{\text{SCE}}^\circ = 0.2415 \text{ V}$ at 25°C .

2.4. Photocatalytic activity for hydrogen evolution

The photocatalytic reaction was carried out in an 80 mL quartz flask equipped with a flat optical entry window. The effective irradiation area for the cell is ca. 3 cm^2 . In a typical photocatalytic experiment, 25 mg of photocatalyst was dispersed in 70 mL of a mixed aqueous solution containing 0.35 M Na_2S and 0.25 M Na_2SO_3 , and the system was deaerated by bubbling argon into the solution for 30 min before light irradiation. A 150 W Xe lamp equipped with a cut-off filter ($\lambda > 400 \text{ nm}$) was used as a visible light source. The lamp was positioned ca. 10 cm away from the optical entry window of the reactor. The produced hydrogen gas was analyzed with an online gas chromatograph (GC1650) equipped with a thermal conductivity detector (TCD) and 5 \AA molecular sieve columns using argon as carrier gas. The standard H_2 -Ar gas mixtures of known concentrations were used for GC signal calibration. The apparent quantum yield (QY) was measured by using GY-10 xenon lamp (150 W) with a 400 nm band-pass filter as light sources. The light intensity on the reactor window was measured by a visible light radiometer (Model: FZ-A, Photoelectric Instrument Factory of Beijing Normal University, China). The light intensity on the reactor window was ca. 5.0 mW cm^{-2} . The apparent quantum yield (QY) of hydrogen is defined by the following Eq. (3):

$$\begin{aligned} \text{Quantum yield (QY)} &= \frac{\text{Number of reacted electrons}}{\text{Number of incident photons}} \times 100\% \\ &= \frac{2 \times n_{\text{H}_2}}{I_0 \times t} \times 100\% \end{aligned} \quad (3)$$

where n_{H_2} is the molar number of evolved hydrogen at time t and I_0 ($I_0 = 1.7 \times 10^{-8} \text{ mol s}^{-1}$) is the molar number of incident photons per second measured at $\lambda = 400 \text{ nm}$.

3. Results and discussion

3.1. Morphology and structure of the samples

Fig. 1 shows the XRD patterns of CdS, NbR, CN_{20} and CN_{20}G_2 . For the CdS sample, the peaks located at 25.0° , 26.6° , 28.3° , 36.7° , 43.9° , 48.0° and 52.0° (curve a) correspond to (100), (002), (101), (102), (110), (103) and (112) planes of the hexagonal structure of CdS, respectively (JCPDS No. 41-1049). The as-prepared NbR sample demonstrates the peaks located at 22.5° , 28.3° , 36.5° , 45.9° , 50.2° , 54.8° , 55.7° and 58.6° (curve b), which can be indexed to (001), (100), (101), (002), (110), (102), (111) and (200) crystal planes of the pure orthorhombic Nb_2O_5 , respectively (T-phase JCPDS, No. 30-0873). In addition, the extraordinary strong intensity of (001) peak indicates that the crystal of Nb_2O_5 has special anisotropic growth along the plane [20,33]. For the CN_{20} nanohybrid, the typical diffraction peaks at 26.6° , 43.9° , 52.0° belonging to CdS and the peaks at 22.5° , 28.3° , 36.5° belonging to Nb_2O_5 can be observed (curve c), demonstrating that $\text{CdS}/\text{Nb}_2\text{O}_5$ hybrid has been successfully synthesized. For the CN_{20}G_2 nanocomposite (curve d), the main diffraction peaks of both CdS and Nb_2O_5 can be detected, however, no typical diffraction peaks belonging to the NGR component can be observed, which can be attributed to the low content and relatively low diffraction intensity of NGR [34].

Fig. 2 shows the SEM images of the NbR and CN_{20} samples and HRTEM image of the CN_{20} sample. From Fig. 2A, it could be seen

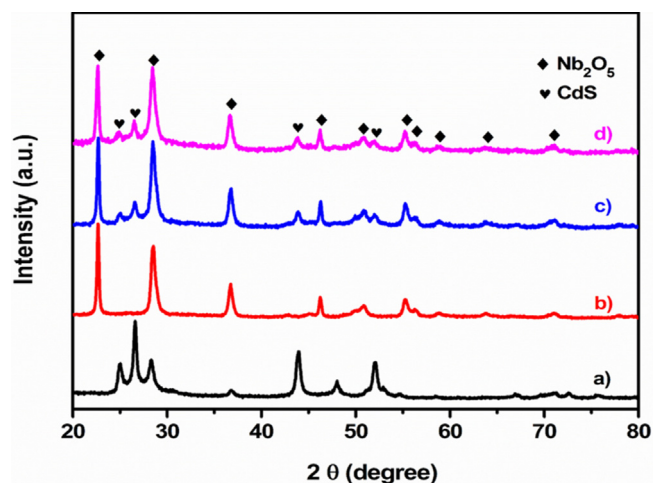


Fig. 1. XRD patterns of the samples of (a) CdS, (b) NbR, (c) CN₂₀ and (d) CN₂₀G₂ nanocomposites.

that as-prepared Nb₂O₅ sample mainly composed of nanorods with an average diameter of approximately 80–120 nm and length of 0.7–1.5 μ m. Compared to NbR, the CN₂₀ sample exhibits a larger diameter and rougher surface (Fig. 2B), indicating the successful deposition of CdS nanoparticles (NPs) on NbR. The morphological and structural features of the CN₂₀ sample were further examined by HRTEM. As demonstrated in the HRTEM image (Fig. 2C), the lattice fringes with d-spacing of 0.357 nm corresponds to the (001) planes of the Nb₂O₅ lattice (T-phase JCPDS, No. 30-0873) and a different kind of lattice fringes with d-spacing of 0.346 nm in the outer

region belongs to the typical (002) planes of cubic structure of CdS (JCPDS No. 41-1049) [35,36]. The STEM elemental mapping of CN₂₀ (Fig. 2D–G) shows the distribution of the Nb, O and Cd elements in a single rod. We can see from the images that the Nb and O elements are main components of the nanorods, whereas the Cd atoms aggregated as NPs are well dispersed on the surface of the Nb₂O₅ rod. These results further demonstrate that the CdS NPs has been decorated on the surface of NbR with a formation of a hetero-junction structure. The image of the CN₂₀G₂ composite is shown in Fig. S1, from which we can see that the CN₂₀ nanorods have been homogeneously distributed on the two-dimensional wrinkled NGR sheets.

Fig. 3 shows the Raman spectra of NbR, CN₂₀, CN₂₀G₂ and NGR. For the pristine NbR, the Raman bands centered at 223 and 689 cm⁻¹ (curve a) are attributed to the symmetric and asymmetric stretching modes of Nb₂O₅ [37–39]. The Raman spectrum of CN₂₀ (curve b) is almost as same as the one of NbR with two peaks centered at 223 and 698 cm⁻¹ except that a weak peak appears ca. 301 cm⁻¹, which is corresponding to the longitudinal optical phonon mode of CdS [40]. Compared with the spectrum of NbR, the peak centered at 698 cm⁻¹ becomes more broadened and demonstrates a blue shift of 9 cm⁻¹, which might attribute to the interaction of CdS NPs with NbR. The similar phenomenon has also been observed by other group from the spectrum of MoS₂ modified TiO₂ nanocomposite [41]. The Raman spectrum of CN₂₀G₂ (curve c) includes typical peaks of both CN₂₀ and NGR. Interestingly, the D band and G band position of NGR in CN₂₀G₂ up-shifts 5 and 6 cm⁻¹ compared with that of the bands of pristine NGR (the inset of Fig. 3), which may be due to the interactions between CN₂₀ and the NGR sheets [25,42].

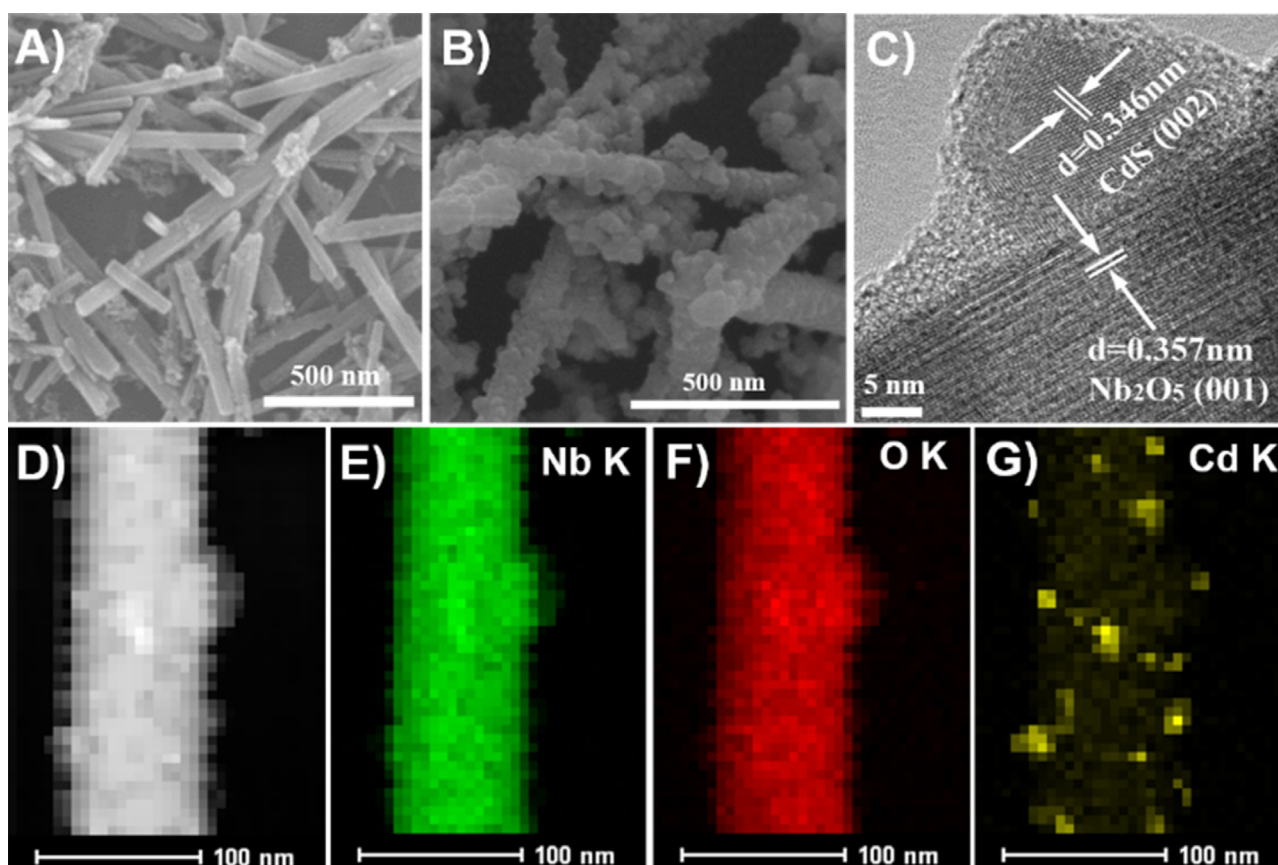


Fig. 2. SEM images of (A) NbR, (B) CN₂₀, (C) HRTEM image of CN₂₀, (D) STEM image of CN₂₀, (E) Nb, (F) O and (G) Cd EDX element mapping of the area of (D).

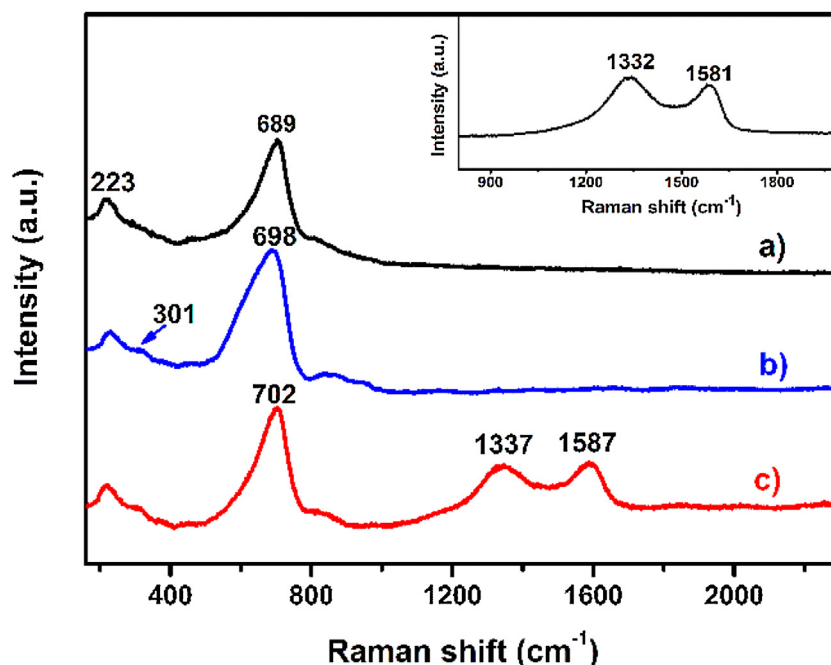


Fig. 3. Raman spectra of (a) NbR, (b) CN_{20} and (c) CN_{20}G_2 . Inset: the plot of NGR.

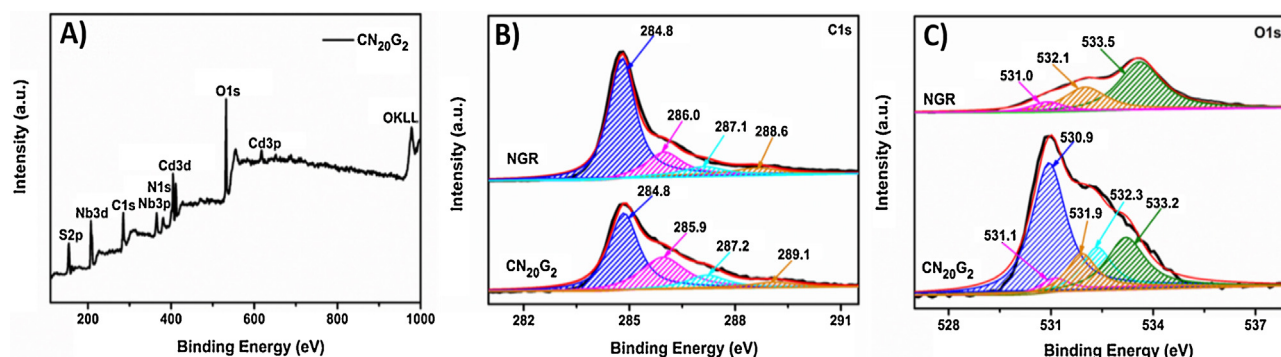


Fig. 4. (A) XPS spectra survey of CN_{20}G_2 , (B) C 1s for NGR and CN_{20}G_2 , (C) O 1s for NGR and CN_{20}G_2 .

Fig. 4A shows the XPS survey spectrum of the CN_{20}G_2 sample, which indicates the sample consists of C, N, Nb, O, Cd and S elements. The high-resolution C 1s XPS spectra of the NGR and CN_{20}G_2 samples are presented in Fig. 4B. The C 1s spectrum of NGR can be deconvoluted into four peaks centered at 284.8, 286.0, 287.1 and 288.6 eV, corresponding to the C–C, C–N/C–O, C=O and O=C–O species, respectively [43]. The C 1s spectrum of CN_{20}G_2 can also be deconvoluted into almost the same four peaks. However, the peak corresponding to the O=C–O species upshifts to 289.1 eV, indicating that some kind of C–O–Cd bond has formed in the composite. The similar phenomenon has also reported by other groups [44,45]. The high-resolution O 1s XPS spectra of the NGR and CN_{20}G_2 samples are presented in Fig. 4C. The three peaks deconvoluted from O 1s spectrum of NGR centered at 531.0, 532.1 and 533.5 eV can be attributed to the C–O, C=O and O=C–O species, respectively [46]. However, the O 1s XPS spectrum of CN_{20}G_2 can be fitted into five peaks centered at 530.9, 531.1, 531.9, 532.3 and 533.2 eV, respectively. The new peak centered at 530.9 eV is closely related to the O element in niobium oxide, while another new peak centered at 532.3 eV could indicate the formation of Cd–O–C bond [47]. For comparison, the XPS spectra of Nb 3d, Cd 3d and S 2p of CN_{20}G_2 are shown in Fig. S2. The spectrum of Nb 3d (Fig. S2A) demonstrates the

two prominent peaks centered at 208.0 and 210.7 eV corresponding to Nb 3d_{5/2} and 3d_{3/2} of Nb_2O_5 , respectively, suggesting that Nb exists in the chemical state of Nb^{5+} . The binding energies of the Cd 3d_{5/2} and Cd 3d_{3/2} at 405.8 and 412.6 eV (Fig. S2B), and the lower bonding energy peaks at 162.2 eV and 163.2 eV of S 2p (Fig. S2C) are consistent with the values reported for CdS [48].

3.2. Optical and photoelectrochemical properties

Fig. 5 shows the UV–vis diffuse reflectance spectra (DRS) of the samples. As shown in Fig. 5A, the pure NbR exhibits an absorption edge at 365 nm. After the CdS NPs (5 wt.%) were decorated onto NbR, a new optical absorption edge extended to 485 nm appears. As the content of CdS NPs in the CdS/ Nb_2O_5 nanohybrid increases, the absorption edge red shifts. The absorption edge of CN_{10} , CN_{20} and CN_{40} is ca. 505, 515 and 530 nm, respectively. Coupling NGR with CdS/ Nb_2O_5 significantly influences the absorbance of the CN_{20}G_y nanocomposites. With the increase of NGR content in the CN_{20}G_y composite, the absorbance intensity in the visible light region ranging from 400 to 800 nm increases obviously (Fig. 5B). This phenomenon demonstrates that coupling NGR with semiconductors may enhance the light harvesting efficiency of the

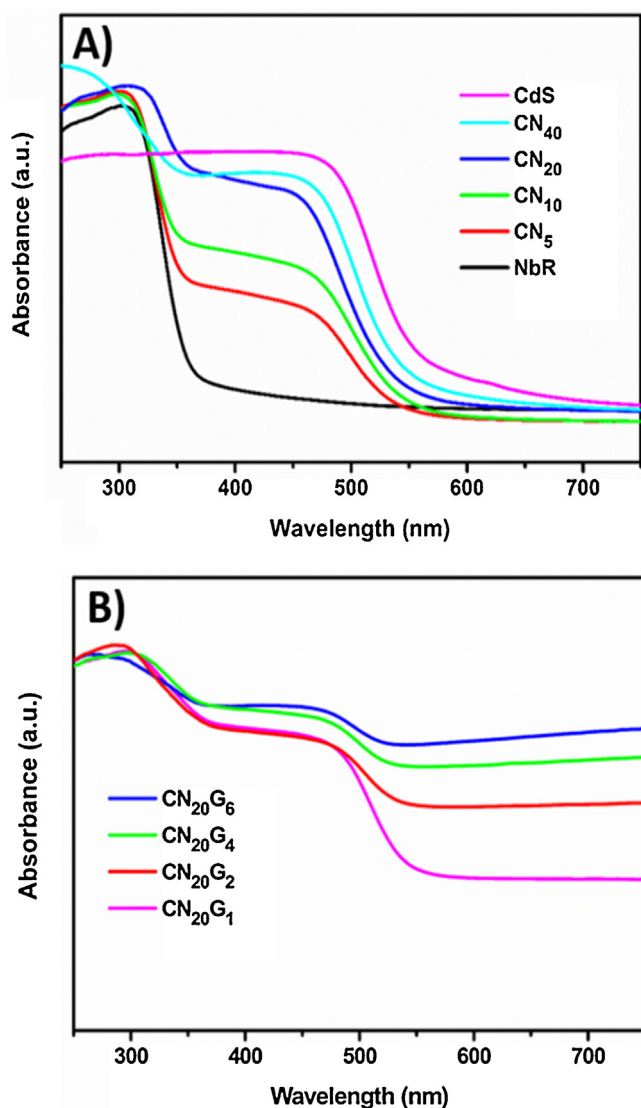


Fig. 5. Comparison of UV-vis diffuse reflectance spectra (DRS) of the various as-prepared (A) NbR, CdS and CdS/Nb₂O₅ nanocomposites, (B) CN₂₀G_y nanocomposites with different compositions.

composites, which in turn will be beneficial for the photocatalysis [12,49]. Moreover, the plots obtained via the transformation based on the Kubelka-Munk function versus the photon energy were shown in Fig. S3. The optical band gap E_g of the as-prepared samples is estimated by extrapolating the linear region of the Kubelka-Munk function plots to the photon energy axis [50], which give the optical band gap of 3.4, 2.4, 2.2 and 2.0 eV for NbR, CN₂₀, CdS and CN₂₀G₂, respectively.

The photocurrent, electrochemical impedance spectra (EIS) and cyclic voltammograms (CVs) of the samples are demonstrated in Fig. 6 to determine the charge carriers transfer in the nanocomposites. As shown in Fig. 6A, the NbR electrode (curve a) did not show photocurrent response under visible irradiation because of its large bandgap energy (3.4 eV), while the photocurrent density of the CdS and CN₂₀ electrode (curve b and c) reached to 0.6 and 0.9 $\mu\text{A cm}^{-2}$, respectively. The enhanced photocurrent density of CN₂₀ may be interpreted as that the hybrid possesses strong visible light absorption and also the heterojunction formed between CdS and NbR increases the transfer and separation efficiency of photogenerated charges [51–53]; while the photocurrent density of the electrode of CdS modified Nb₂O₅ NPs was 0.61 $\mu\text{A cm}^{-2}$

(Fig. S5A) under same conditions, lower than that of the CN₂₀ electrode, apparently owing to morphology effect of the 1D NbR. The photocurrent responses for the CN₂₀G₂ electrode (curve d) are prompt, steady and reproducible during the chopped visible light illumination. The highest photocurrent intensity (1.7 $\mu\text{A cm}^{-2}$) of the CN₂₀G₂ electrode demonstrates that NGR in the nanocomposite serves as an acceptor and a transporter for the electrons generated from the CN₂₀ hybrid, inhibiting the recombination of photoinduced electron-holes effectively [24,54,55]. Fig. 6B is shown the EIS presented as Nyquist plots of the as-prepared samples. In the equivalent Randle circuit, R_s is the solution resistance, Q is the capacitance of the electrode/electrolyte double layer, R_{ct} is the charge transfer resistance across the interface of electrode/electrolyte, which can be expressed as the diameter of the semicircle in the Nyquist plot, and W is the Warburg impedance. The diameter of the Nyquist curves of the samples changes in the order: NbR (198 Ω) > CdS (180 Ω) > CN₂₀ (175 Ω) > CN₂₀G₂ (90 Ω), demonstrating that the CN₂₀G₂ electrode possesses the lowest resistance and the highest charge transfer efficiency at the interface of the electrode/electrolyte. As shown in Fig. 6C, the CVs results of the electrodes covered with the as-prepared samples measured at a scan rate of 20 mV s^{-1} show clear anodic and cathodic peaks for each sample. The NbR, CdS, CN₂₀ and CN₂₀G₂ electrode demonstrated a clear cathodic peak at ca. 0.15, 0.13, 0.13 and 0.12 V vs. SCE, respectively. The relative cathodic currents about the peaks were -1.12 , -0.93 , -1.16 and -1.46 mA cm^{-2} , respectively. The fact that CN₂₀G₂ electrode has a higher cathodic current and a lower onset potential of proton reduction than the NbR and CN₂₀ electrodes, which demonstrates that NGR as an electron acceptor can effectively promote charge transfer and decrease the recombination of electron-hole pairs [56,57]. The Mott-Schottky (M-S) plots of NbR, CdS and CN₂₀, CN₂₀G₂ are demonstrated in Figs. 6D and S4, respectively. As expected, all samples show a positive slope as *n*-type semiconductors. Based on the M-S equation, the calculated flat band potential (E_{fb}) of NbR, CdS, CN₂₀ and CN₂₀G₂ at the measured conditions is ca. -0.73 , -0.87 , -0.75 and -0.70 V vs. SCE (-0.13 , -0.27 , -0.15 and -0.10 V vs. RHE), respectively. Since the flat band potential of the *n*-type semiconductors may be considered approximately as the conduction band edge [58], the potential gradient produced in the hybrid at the interface between CdS and NbR may facilitate the photoexcited electrons transfer from CdS moiety to NbR and enhance charges separation efficiency. The potentials of the conduction band and calculated valence band values, together with the band gaps got from the Kubelka-Munk function plots are listed in Table S1.

3.3. Photocatalytic performances

The photocatalytic performances for hydrogen production over NbR, CdS and the CdS/Nb₂O₅ nanohybrids under visible light irradiation ($>400 \text{ nm}$) are shown in Fig. 7A. NbR basically does not produce measurable hydrogen under visible light irradiation because of its large bandgap energy (3.4 eV). The amount of H₂ evolved from pure CdS under 8 h visible light irradiation is 104 $\mu\text{mol g}^{-1}$ while the amount of H₂ evolved from CN₅ is 159 $\mu\text{mol g}^{-1}$, indicating a positive effect on the enhancement of the photocatalytic activity by coupling CdS NPs with NbR. As the amount of CdS NPs increases in the hybrid, the photocatalytic activity of the CdS/Nb₂O₅ hybrids increases. The amount of H₂ evolved from CN₂₀ under 8 h visible light irradiation reaches to 420 $\mu\text{mol g}^{-1}$, which is ca. 4.0 and 2.0 times as high as that of pure CdS and CdS/Nb₂O₅ NPs (Fig. S5B) under the same reaction conditions. This enhancement in photocatalytic activity might be attributed to the heterojunction structures formed between CdS NPs and NbR, which promote the photogenerated electron transfer from CdS NPs to 1D Nb₂O₅ nanorods and hinder the charges

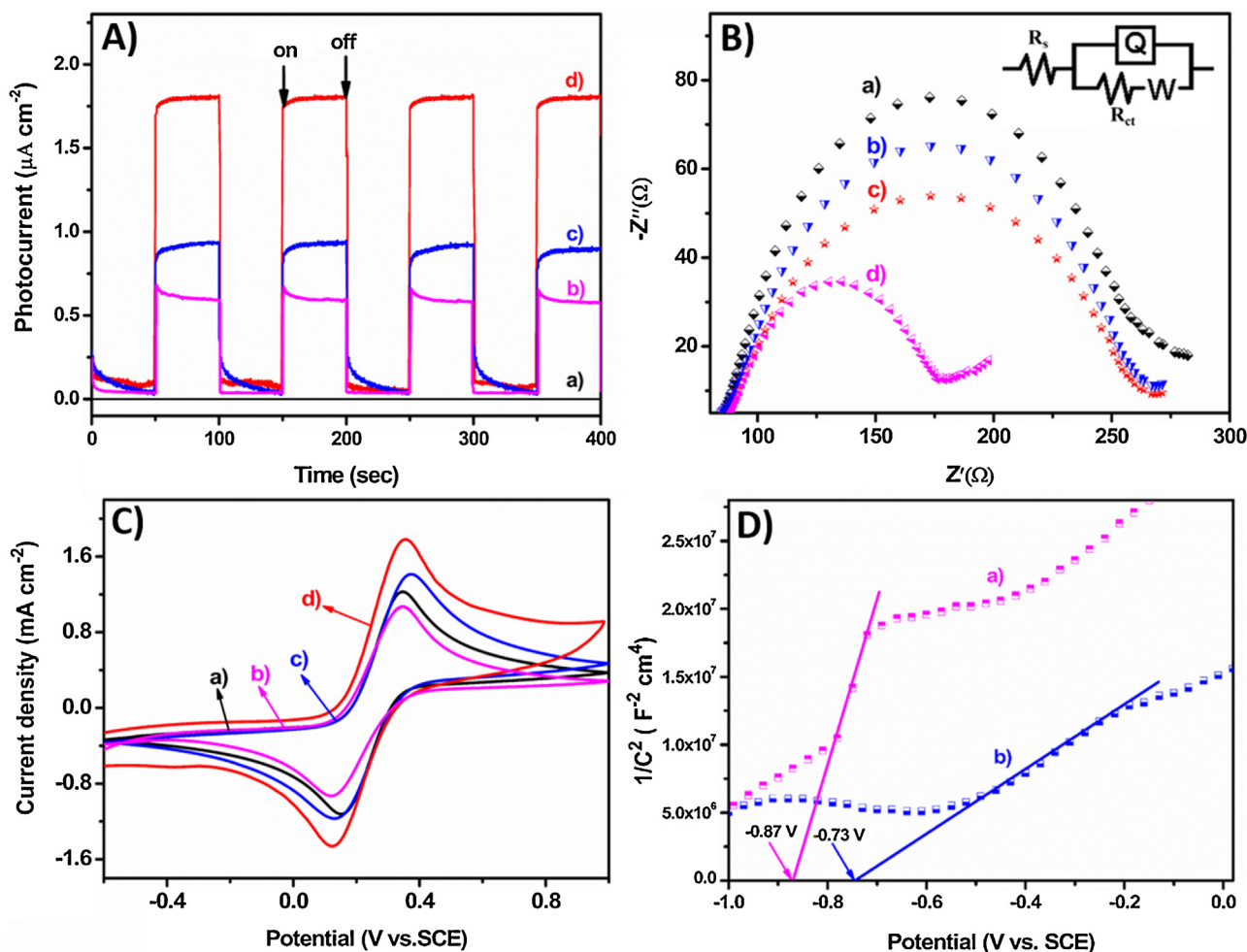


Fig. 6. (A) Photocurrent of (a) NbR, (b) CdS, (c) CN₂₀ and (d) CN₂₀G₂ electrode under visible light irradiation at 0.4 V vs. SCE. The illumination from a Xe lamp equipped with a cut-off filter ($\lambda > 400$ nm) was interrupted every 50 s. (B) EIS spectra of (a) NbR, (b) CdS, (c) CN₂₀ and (d) CN₂₀G₂ electrode in 5.0 mM K₃[Fe(CN)₆]/K₄[Fe(CN)₆] solution at a potential of 0.2 V vs. SCE. The inset shows an equivalent circuit for the electrode. (C) CVs of (a) NbR, (b) CdS, (c) CN₂₀ and (d) CN₂₀G₂ electrode in 5.0 mM K₃[Fe(CN)₆]/K₄[Fe(CN)₆] and 0.2 M KCl solution at a scan rate of 20 mV s⁻¹. (D) Mott-Schottky plots of (a) CdS and (b) NbR electrode measured in 0.2 M Na₂SO₄ (pH = 6) solution at an applied frequency of 1000 Hz.

recombination. Besides, the Nb₂O₅ nanorods in the nanohybrid with high surface to volume ratio also provide a direct path for photoinduced charges transfer. However, higher loading CdS NPs on NbR decreases the photocatalytic activity. The amount of H₂ evolved from CN₄₀ under 8 h visible light irradiation decreases to 337 μmol g⁻¹, which can be attributed to that the photocatalytic effect of the CdS/Nb₂O₅ hybrid becomes less remarkable as the ratio of the CdS NPs in the hybrid increases to some extent.

Corporation of NGR with CN₂₀ obviously increases photocatalytic activity and the results are shown in Fig. 7B. Under 8 h visible light irradiation, the amount of H₂ evolved from the CN₂₀G₁ catalyst is 569 μmol g⁻¹. The composite catalyst with 2 wt.% NGR (CN₂₀G₂) showed the best performance and the hydrogen amount evolved from the catalyst reached to 800 μmol g⁻¹ under 8 h visible light irradiation, which is ca. 7.7, 3.5 and 1.9 times as high as that evolved from bare CdS, CG₂ and CN₂₀, respectively. The calculated apparent quantum yield (QY) for CN₂₀G₂ at 400 nm according to Eq. (3) is 1.5%. The enhancement of the H₂ production from the optimized composite catalyst can be attributed to the facile electron transfer from photoexcited the CN₂₀ hybrid to NGR nanosheets via the interface of the two moieties, which can prolong the lifetime of carriers. NGR in the nanocomposite as an electron acceptor and transporter is helpful in tailoring the electrons transfer from the CN₂₀ hybrid to the NGR nanosheets and promote the charge separa-

tion, leading to the enhancement of hydrogen evolution. However, when excessive NGR was incorporated in the composite, photocatalytic activity decreased. The total amount of H₂ produced from CN₂₀G₄ and CN₂₀G₆ under 8 h visible light irradiation is 666 and 526 μmol g⁻¹, respectively, which may be attributed to that the overdose NGR in the nanocomposite may produce a filter effect or block the active sites of nanocomposites [59,60]. The influence of the wavelength of the incident light on hydrogen evolution of the CN₂₀G₂ photocatalyst are shown in Fig. 7C. The amount of H₂ evolved from CN₂₀G₂ under 8 h monochromatic visible-light irradiation at 420, 440, 460, 475, 496, 515 and 540 nm was 6.8, 6.4, 5.8, 4.5, 4.0, 2.7 and 2.6 μmol g⁻¹, respectively. The outline of the hydrogen evolution *via* the wavelength of the incident light was consisted with that of the diffuse reflectance spectrum of CN₂₀G₂, indicating that the photocatalytic activity of CN₂₀G₂ was fully correlated with the absorbed light.

The stability of CN₂₀G₂ for H₂ evolution was evaluated by performing recycling experiments under visible light irradiation. As shown in Fig. 8, the amount of H₂ evolved from CN₂₀G₂ is about 3856 μmol g⁻¹ in the total 40 h recycle experiment, and the average production rate of H₂ is about 96.4 μmol g⁻¹ h⁻¹. This result indicates the hetero-structural CN₂₀G₂ catalyst possesses sufficient stability for photocatalytic H₂ evolution.

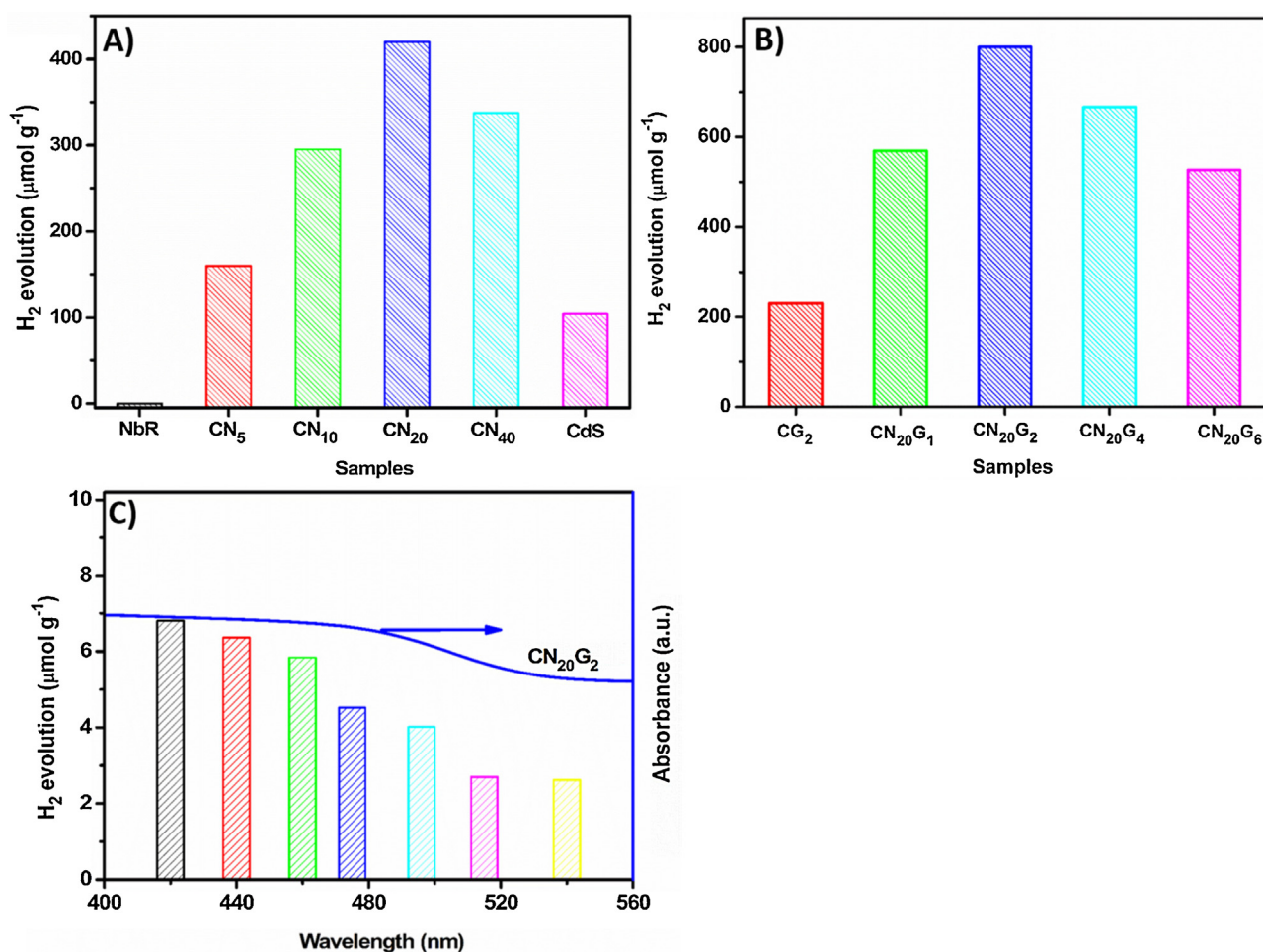


Fig. 7. (A) Hydrogen evolution amounts over various CdS/Nb₂O₅ nanohybrid, (B) The effect of NGR on the amount of H₂ evolved from the CG₂ and CN₂₀G_y nanocomposites photocatalyst under 8 h visible light irradiation. Reaction conditions: $m_{\text{catalyst}} = 25$ mg, $T = 25^\circ\text{C}$, and light.

source: 150 W Xe lamp equipped with a cut-off filter ($\lambda > 400$ nm). (C) The influence of the wavelength of the incident light on hydrogen evolution of the CN₂₀G₂ photocatalyst. Reaction conditions: $m_{\text{catalyst}} = 25$ mg, $T = 25^\circ\text{C}$.

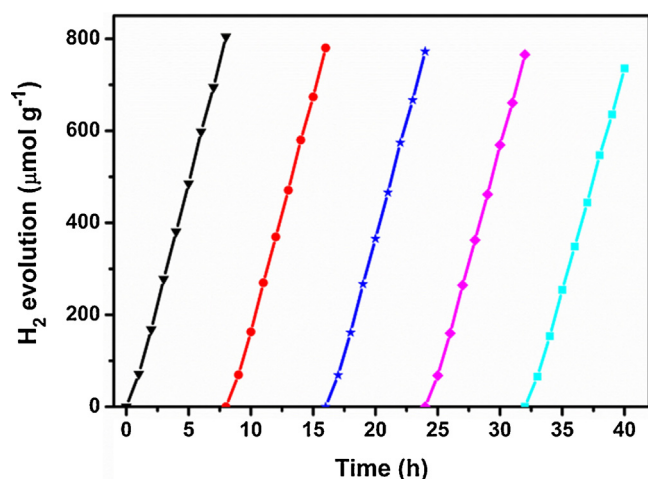


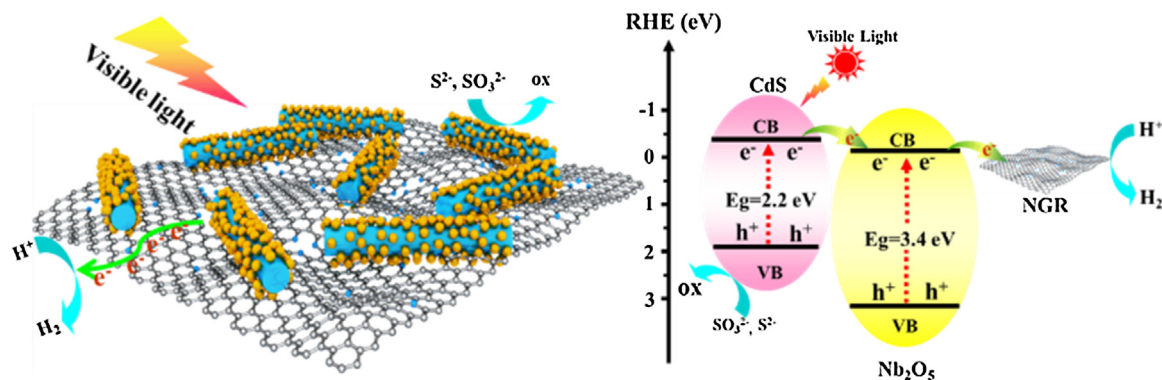
Fig. 8. Cycling measurements of the amount of H₂ evolved under visible light irradiation by CN₂₀G₂ composite. Reaction conditions: $m_{\text{catalyst}} = 25$ mg, $T = 25^\circ\text{C}$, light. source: 150 W Xe lamp ($\lambda > 400$ nm).

A tentative mechanism proposed for the H₂ production over CN₂₀G₂ is illustrated in Scheme 2. Under visible light irradiation, the electrons are photoexcited from valence band (VB) of the narrow bandgap CdS (2.2 eV) to its conduction band (CB, -0.27 V vs.

RHE), then transfer towards the CB (-0.13 V vs. RHE) of NbR. The heterojunction structures formed between the two moieties promote the photogenerated electrons transfer and hinder the charges recombination. The electrons in CB of NbR then migrate to the NGR (-0.08 V vs. RHE) [61] nanosheets and react with H⁺ forming H₂. The holes in the VB of CdS transfer to the surface and react with holes scavengers of S²⁻ or SO₃²⁻.

4. Conclusions

In summary, we have successfully developed a novel visible-light-driven photocatalysts by depositing 0D CdS NPs on 1D Nb₂O₅ nanorods to form a hybrid and then incorporating the hybrid with 2D NGR forming a hetero-structural nanocomposite. Under visible light ($\lambda > 400$ nm) irradiation, the as-prepared ternary nanocomposites displayed high efficiency for the photocatalytic H₂ evolution. The amount of H₂ evolved from the optimal photocatalyst (CN₂₀G₂) is 800 μmol g⁻¹ under 8 h visible light irradiation, which is ca. 7.7 and 3.5 times as high as that evolved from bare CdS and CG₂, respectively. The enhancement of photocatalytic performances were attributed to the unique 1D Nb₂O₅ structure with high surface-to-volume ratio, which can provide intimate interfacial contact between NbR and CdS nanoparticles, the CdS/Nb₂O₅ heterojunction, and excellent electronic conductivity of NGR. This investigation provides a promising and cost-effective approach to



Scheme 2. Schematic illustration of the charge transfer in CN_xG_y nanocomposites.

construct highly efficient photocatalytic hydrogen evolution system without using any noble metal.

Acknowledgments

The authors gratefully acknowledge financial support of this research by the National Natural Science Foundation of China (21373143) and the Priority Academic Program Development of Jiangsu Higher Education Institutions (PAPD).

Appendix A. Supplementary data

Supplementary data associated with this article can be found, in the online version, at <http://dx.doi.org/10.1016/j.apcatb.2016.08.028>.

References

- [1] X. Chen, S. Shen, L. Guo, S.S. Mao, *Chem. Rev.* 110 (2010) 6503–6570.
- [2] K. Maeda, K. Teramura, D. Lu, T. Takata, N. Saito, Y. Inoue, K. Domen, *Nature* 440 (2006), 295–295.
- [3] S.U.M. Khan, M. Al-Shahry, W.B. Ingler, *Science* 297 (2002) 2243–2245.
- [4] A. Fujishima, K. Honda, *Nature* 238 (1972) 37–38.
- [5] X. Zong, H. Yan, G. Ma, F. Wen, L. Wang, C. Li, *J. Am. Chem. Soc.* 130 (2008) 7176–7177.
- [6] A. Kudo, Y. Miseki, *Chem. Soc. Rev.* 38 (2009) 253–278.
- [7] X. Zong, J. Han, G. Ma, H. Yan, G. Wu, C. Li, *J. Phys. Chem. C* 115 (2011) 12202–12208.
- [8] Q. Xiang, B. Cheng, J. Yu, *Appl. Catal. B* 138–139 (2013) 299–303.
- [9] Y. Zhang, Y. Tang, X. Liu, Z. Dong, H.H. Hng, Z. Chen, T.C. Sum, X. Chen, *Small* 9 (2013) 996–1002.
- [10] Y. Chen, L. Wang, G. Lu, X. Yao, L. Guo, *J. Mater. Chem.* 21 (2011) 5134–5141.
- [11] X. Zou, P.P. Wang, C. Li, J. Zhao, D. Wang, T. Asefa, G.D. Li, *J. Mater. Chem. A* 2 (2014) 4682–4689.
- [12] X. Wang, X. Yao, *Carbon* 77 (2014) 667–674.
- [13] C. Han, Z. Chen, N. Zhang, J.C. Colmenares, Y.J. Xu, *Adv. Funct. Mater.* 25 (2015) 221–229.
- [14] J. Hou, Z. Wang, W. Kan, S. Jiao, H. Zhu, R.V. Kumar, *J. Mater. Chem.* 22 (2012) 7291–7299.
- [15] P. Gao, J. Liu, S. Lee, T. Zhang, D.D. Sun, *J. Mater. Chem.* 22 (2012) 2292–2298.
- [16] H. Huang, C. Wang, J. Huang, X. Wang, Y. Du, P. Yang, *Nanoscale* 6 (2014) 7274–7280.
- [17] Z. Yue, D. Chu, H. Huang, J. Huang, P. Yang, Y. Du, M. Zhu, C. Lu, *RSC Adv.* 5 (2015) 47117–47124.
- [18] X. Chen, T. Yu, X. Fan, H. Zhang, Z. Li, J. Ye, Z. Zou, *Appl. Surf. Sci.* 253 (2007) 8500–8506.
- [19] C. Yan, D. Xue, *Adv. Mater.* 20 (2008) 1055–1058.
- [20] Y. Zhao, C. Eley, J. Hu, J.S. Foord, L. Ye, H. He, S.C.E. Tsang, *Angew. Chem. Int. Ed.* 51 (2012) 3846–3849.
- [21] B. Gao, J. Fu, K. Huo, W. Zhang, Y. Xie, P.K. Chu, *J. Am. Ceram. Soc.* 94 (2011) 2330–2338.
- [22] F. Meng, J. Li, S.K. Cushing, M. Zhi, N. Wu, *J. Am. Chem. Soc.* 135 (2013) 10286–10289.
- [23] Y. Shao, S. Zhang, M.H. Engelhard, G. Li, G. Shao, Y. Wang, J. Liu, I.A. Aksay, Y. Lin, *J. Mater. Chem.* 20 (2010) 7491–7496.
- [24] H. Wang, T. Maiyalagan, X. Wang, *ACS Catal.* 2 (2012) 781–794.
- [25] Z. Mou, Y. Wu, J. Sun, P. Yang, Y. Du, C. Lu, *ACS Appl. Mater. Interfaces* 6 (2014) 13798–13806.
- [26] X. Li, H. Wang, J.T. Robinson, H. Sanchez, G. Diankov, H. Dai, *J. Am. Chem. Soc.* 131 (2009) 15939–15944.
- [27] L. Qu, Y. Liu, J.B. Baek, L. Dai, *ACS Nano* 4 (2010) 1321–1326.
- [28] L. Lai, J.R. Potts, D. Zhan, L. Wang, C.K. Poh, C. Tang, H. Gong, Z. Shen, J. Lin, R.S. Ruoff, *Energy Environ. Sci.* 5 (2012) 7936–7942.
- [29] L. Jia, D.H. Wang, Y.X. Huang, A.W. Xu, H.Q. Yu, *J. Phys. Chem. C* 115 (2011) 11466–11473.
- [30] C. Luo, D. Xue, *Langmuir* 22 (2006) 9914–9918.
- [31] F. Cardon, W.P. Gomes, *J. Phys. D: Appl. Phys.* 11 (1978) L63.
- [32] S. Shen, J. Jiang, P. Guo, C.X. Kronawitter, S.S. Mao, L. Guo, *Nano Energy* 1 (2012) 732–741.
- [33] Y. Zhou, Z. Qiu, M. Lü, A. Zhang, Q. Ma, *J. Lumin.* 128 (2008) 1369–1372.
- [34] Q. Li, B. Guo, J. Yu, J. Ran, B. Zhang, H. Yan, J.R. Gong, *J. Am. Chem. Soc.* 133 (2011) 10878–10884.
- [35] C. Yan, L. Nikolova, A. Dadvand, C. Harnagea, A. Sarkissian, D.F. Perepichka, D. Xue, F. Rosei, *Adv. Mater.* 22 (2010) 1741–1745.
- [36] J. Yu, J. Zhang, M. Jaroniec, *Green Chem.* 12 (2010) 1611–1614.
- [37] M.S.P. Francisco, Y. Gushikem, *J. Mater. Chem.* 12 (2002) 2552–2558.
- [38] S. Xie, E. Iglesia, A.T. Bell, *J. Phys. Chem. B* 105 (2001) 5144–5152.
- [39] P. Arunkumar, A.G. Ashish, B. Babu, S. Sarang, A. Suresh, C.H. Sharma, M. Thalakkulam, M.M. Shaijumon, *RSC Adv.* 5 (2015) 59997–60004.
- [40] S. Rengaraj, S. Venkataraj, S.H. Jee, Y. Kim, C.W. Tai, E. Repo, A. Koistinen, A. Ferencova, M. Sillanpää, *Langmuir* 27 (2011) 352–358.
- [41] M. Shen, Z. Yan, L. Yang, P. Du, J. Zhang, B. Xiang, *Chem. Commun.* 50 (2014) 15447–15449.
- [42] Y. Wu, D. Chu, P. Yang, Y. Du, C. Lu, *Catal. Sci. Technol.* 5 (2015) 3375–3382.
- [43] G. Zhou, E. Paek, G.S. Hwang, A. Manthiram, *Nat. Commun.* 6 (2015) 1–11.
- [44] Q. Xiang, J. Yu, M. Jaroniec, *Nanoscale* 3 (2011) 3670–3678.
- [45] J. Sun, H. Zhang, L.H. Guo, L. Zhao, *ACS Appl. Mater. Interfaces* 5 (2013) 13035–13041.
- [46] B. Khare, P. Wilhite, B. Tran, E. Teixeira, K. Fresquez, D.N. Mvondo, C. Bauschlicher, M. Meyyappan, *J. Phys. Chem. B* 109 (2005) 23466–23472.
- [47] T. Lu, R. Zhang, C. Hu, F. Chen, S. Duo, Q. Hu, *Phys. Chem. Chem. Phys.* 15 (2013) 12963–12970.
- [48] W.J. Jiang, Y.F. Liu, R.L. Zong, Z.P. Li, W.Q. Yao, Y.F. Zhu, *J. Mater. Chem. A* 3 (2015) 18406–18412.
- [49] X. Wang, G. Liu, G.Q. Lu, H.-M. Cheng, *Int. J. Hydrogen Energy* 35 (2010) 8199–8205.
- [50] C.S. Pana, J. Xua, Y. Chen, Y.F. Zhu, *Appl. Catal. B* 115–116 (2012) 314–319.
- [51] G. Liu, L. Wang, H.G. Yang, H.M. Cheng, G.Q. Lu, *J. Mater. Chem.* 20 (2010) 831–843.
- [52] L. Xu, J. Guan, W. Shi, *ChemCatChem* 4 (2012) 1353–1359.
- [53] Y.C. Chen, Y.C. Pu, Y.J. Hsu, *J. Phys. Chem. C* 116 (2012) 2967–2975.
- [54] L. Jia, D.H. Wang, Y.X. Huang, A.W. Xu, H.Q. Yu, *J. Phys. Chem. C* 115 (2011) 11466–11473.
- [55] T.G. Xu, L.W. Zhang, H.Y. Cheng, Y.F. Zhu, *Appl. Catal. B* 101 (2011) 382–387.
- [56] X. Pan, Y. Zhao, S. Liu, C.L. Korzeniewski, S. Wang, Z. Fan, *ACS Appl. Mater. Interfaces* 4 (2012) 3944–3950.
- [57] M. Jahan, Z. Liu, K.P. Loh, *Adv. Funct. Mater.* 23 (2013) 5363–5372.
- [58] R. Saito, Y. Miseki, K. Sayama, *Chem. Commun.* 48 (2012) 3833–3835.
- [59] J. Yu, J. Jin, B. Cheng, M. Jaroniec, *J. Mater. Chem. A* 2 (2014) 3407–3416.
- [60] G.K. Pradhan, D.K. Padhi, K.M. Parida, *ACS Appl. Mater. Interfaces* 5 (2013) 9101–9110.
- [61] J. Zhang, J. Yu, Y. Zhang, Q. Li, J.R. Gong, *Nano Lett.* 11 (2011) 4774–4779.